metals

MDPI

Article

Mechanism of Vanadium–Titanium Slag in Regulating the Performance and Hydration of Metallurgical Slag-Based Cementitious Materials

Bo Su [1], Siqi Zhang [1,2,*], Xingyang Xu [2], Tong Zhao [2], Huifen Yang [2] and Junyao Liu [2]

[1] Institute of Mineral Resources, University of Science and Technology Beijing, Beijing 100083, China; ustb_subo@163.com
[2] School of Resources and Safety Engineering, University of Science and Technology Beijing, Beijing 100083, China; 18355781752@163.com (X.X.); d202310038@xs.ustb.edu.cn (T.Z.); yanghf@ustb.edu.cn (H.Y.); 15933769317@163.com (J.L.)
* Correspondence: zsq2017@ustb.edu.cn

Abstract

To achieve the large-scale, high-value utilization of vanadium–titanium slag (VTS) in the metallurgical industry, this study replaces blast furnace slag (BFS) with VTS to construct a quaternary all-solid-waste cementitious system composed of VTS, BFS, steel slag (SS), and desulfurization gypsum (DG). It systematically investigates the effects of VTS content (0–60%) on the mechanical properties, leaching toxicity, and hydration heat behavior of the system. XRD, TG–DSC, and SEM–EDS techniques are employed to explore the influence of VTS on hydration behavior and microstructural evolution. The results show that when VTS replaces 30% of the BFS (A3, VTS:BFS:SS:DG = 3:3:3:1), the 28-day compressive strength reaches 31.33 MPa. The leaching concentrations of heavy metals in all specimens are far below the standards for drinking water quality. Hydration heat analysis reveals that the incorporation of VTS advances the acceleration period of hydration. The A3 specimen maintains a relatively high heat release rate in the middle and later stages (after 72 h), and its cumulative heat release is significantly higher than that of the system without VTS, revealing the "slow hydration" mechanism of VTS at later stages. The $[SiO_4]$–$[AlO_4]$ bonds in VTS undergo a depolymerization–repolymerization process. In addition, an appropriate amount of VTS promotes the deposition of hydration products such as ettringite (AFt), C–S–H, and C–A–S–H gels through micro-filling effects and heterogeneous nucleation, thereby improving the microstructure of the system. However, excessive VTS ($\geq$45%) significantly inhibits the hydration reaction and reduces gel formation due to the decrease in highly reactive BFS components and the increased TiO_2 content. This study provides new insights into the resource utilization of VTS in multi-solid-waste cementitious materials. In addition, VTS-based cementitious materials are suitable for practical scenarios with low early strength requirements, such as goaf backfilling. Therefore, future studies should further investigate the long-term sulfate resistance and carbonation resistance of these materials under real application conditions.

Keywords: vanadium–titanium slag; cementitious materials; hydration mechanism; micro-filling effect; hydration heat; heterogeneous nucleation

Check for updates

Academic Editor: Petros E. Tsakiridis

Received: 23 March 2026
Revised: 12 April 2026
Accepted: 14 April 2026
Published: 18 April 2026

Copyright: © 2026 by the authors. Licensee MDPI, Basel, Switzerland. This article is an open access article distributed under the terms and conditions of the Creative Commons Attribution (CC BY) license.

1. Introduction

Vanadium–titanium magnetite is the primary source of vanadium, titanium, and iron. According to statistics, China's reserves are approximately 18 billion tons [1]. Vanadium–

Titanium slag (VTS) is a bulk metallurgical solid waste generated during the smelting of vanadium–titanium magnetite, with an annual output of up to 5 million tons [2]. VTS typically contains certain proportions of CaO, SiO_2, and Al_2O_3, along with a relatively high content of TiO_2 [3]. Its chemical composition shows certain similarities to that of some cementitious materials, and therefore it theoretically possesses potential cementitious activity [4]. However, the presence of TiO_2 in VTS enhances the stability of the glassy structure [5], making the [SiO_4] and [AlO_4] networks in VTS more difficult to depolymerize and thereby inhibiting early-stage hydration reactions [2,6]. This characteristic poses significant challenges for the large-scale resource utilization of VTS. At present, VTS is mainly managed through storage, which directly occupies land resources. In addition, VTS contains elements such as Ti, and its stockpiling can easily cause pollution to land and water resources, posing potential environmental risks [7]. Therefore, developing high-value resource utilization technologies for VTS has become an important research topic.

In recent years, the use of VTS as a supplementary material in cement-based materials has become a research hotspot in the building materials field [8,9]. Liu et al. [7] used titanium extraction slag (TES) to mitigate the strength reduction of calcium aluminate cement (CAC). The study found that adding 30% TES generated layered double hydroxides and transformed C–S–H into C–A–S–H, thereby improving the compressive strength. Liu et al. [6] enhanced the workability of magnesium phosphate cement (MPC) and reduced its hydration heat by adding titanium slag. The study shows that when the titanium slag content is 50%, MPC samples with M/P ratios of 2:1 and 3:1 exhibit significantly higher fluidity than the control group, with initial setting times extended by 115.4% and 100%, and hydration temperatures reduced by 21.9% and 17%, respectively. When the titanium slag content is 30%, the sample with M/P = 3:1 displays a dense structure and high strength. Ma et al. [2] prepared a novel low-carbon fire-resistant cementitious composite with good high-temperature performance using titanium slag (TS) and fly ash. The results show that an appropriate addition of TS reduces mass loss by 19.6% and decreases the degree of mechanical strength degradation by 31.8% after heating at 800 °C. The thermally stable perovskite and akermanite phases in TS contribute to the stability of mineral phases during high-temperature heating. In addition, TS particles effectively optimize the internal pore distribution and limit the formation and deterioration of large pores. Li et al. [10] used titanium slag (TS) as a replacement aggregate to prepare reactive powder concrete (RPC) and investigated its mechanical properties, hydration, and interfacial microstructure. The results show that the porous, low-reactivity TS aggregate exhibits high adsorption and appropriate secondary hydration during molding and hardening. This accelerates the early hydration of RPC and significantly improves the interfacial structure between the paste and the aggregate. He et al. [11] prepared a soil–cement–bentonite (SCB) slurry using cement, clay, bentonite, and reactive high-titanium slag (HTS). The results show that when HTS replaces 50% of the cement, the HTS-SCB slurry exhibits optimal impermeability, appropriate mechanical properties, and low risk of heavy metal leaching. Rui et al. [4] compared the chemical composition of VTS and blast furnace slag (BFS) and their hydration behavior in Portland cement. They found that the main components and morphologies of VTS and BFS are similar. The flowability of cement-based materials containing VTS and BFS shows little difference. From the perspective of hydration heat, the excessively high Ti content in VTS inhibits the hydration of BFS and cement. Based on long-term hydration and microstructural tests, it is evident that highly crystalline VTS is unfavorable for the formation of hydration products and the densification of the microstructure, leading to increased porosity. The above studies provide theoretical support for the use of VTS in the preparation of construction materials.

In addition, to align with green and low-carbon development, the synergistic utilization of metallurgical by-products such as BFS, steel slag (SS), and desulfurization gypsum (DG) in the construction materials field has become an important research topic [12–14]. BFS is a typical latent hydraulic material that is rich in amorphous silico-aluminate glass. Under appropriate activation conditions, it can undergo hydration reactions to form cementitious products such as C–S–H or C–(A)–S–H [15,16]. However, the hydration rate of a sole BFS system is relatively slow and requires external activators to enhance its reactivity [13]. SS, as an important by-product of the steelmaking process, contains a high content of free CaO and C_2S in its mineral composition [17]. During hydration, it can release Ca^{2+} and OH^- and provide an alkaline environment [18], thereby partially activating the latent hydraulic activity of BFS. In addition, DG, as a by-product of flue gas desulfurization in coal-fired power plants, mainly consists of $CaSO_4 \cdot 2H_2O$. It can provide a source of SO_4^{2-} for the cementitious system and promote the formation of ettringite (AFt) [19]. The above studies provide theoretical feasibility for the synergistic use of VTS with other solid wastes to prepare solid-waste-based cementitious materials. The study [20] shows that under alkaline conditions and sulfate activation, VTS-based cementitious systems can form hydration products such as AFt, C–S–H, and C–A–S–H gels.

However, few studies have reported on the performance and hydration mechanism of VTS-based cementitious materials. In particular, the role of VTS in BFS–SS–DG composite cementitious systems still lacks systematic investigation. First, the appropriate dosage range of VTS in multi-solid-waste systems remains unclear, and excessive replacement of slag may lead to the strength deterioration of the system [4]. In addition, the hydration behavior of VTS differs fundamentally from that of ordinary slag. In particular, the high content of TiO_2 and the stable crystalline phases in VTS may significantly affect the hydration reactions of the system. However, few studies have reported the feasibility of using VTS in combination with other solid wastes to prepare cementitious materials. This limitation restricts the understanding of the hydration mechanisms of VTS and hinders research on its resource utilization. Finally, the environmental safety of VTS-based cementitious systems, such as the risk of heavy metal leaching, urgently needs to be assessed. Therefore, it is necessary to conduct in-depth studies using multi-scale characterization techniques to investigate the role of VTS in the BFS–SS–DG system, in order to reveal its effects on hydration kinetics and microstructural evolution. This is of significant engineering value and scientific importance for achieving the large-scale, low-cost utilization of VTS.

Based on the above background, this study replaces BFS with VTS to construct a quaternary all-solid-waste cementitious system composed of VTS, BFS, SS, and DG. First, it systematically investigates the effects of VTS content (0–60%) on the mechanical properties and environmental safety of the system. Secondly, by employing a variety of characterization techniques, including hydration exothermic analysis, X-ray diffraction (XRD), Fourier-transform infrared spectroscopy (FT-IR), thermogravimetric analysis (TG–DSC), X-ray photoelectron spectroscopy (XPS) and scanning electron microscopy (SEM), a comprehensive analysis of the formation of hydration products and changes in microstructure within the system was conducted, thereby elucidating the mechanism of action of VTS in this system. This study provides a theoretical basis for the high-value utilization of VTS in low-carbon cementitious materials.

2. Materials and Methods

2.1. Raw Material

The raw materials are mainly obtained from VTS, BFS, SS, and DG produced by a steel enterprise in Guizhou, China. Among them, VTS is secondary smelting slag after the vanadium extraction process. It serves both as a cementitious material and as

a partial aggregate. According to the standard GB/T 208-2014 [21] "Method for Determination of Cement Density," the density of VTS is determined to be 3.09 kg/m^3. The above raw materials are dried, ground using an SM500 × 500 5 kg laboratory ball mill (Hangzhou Instrument Co., Ltd., Hangzhou, China), and then sealed for subsequent use. The main chemical compositions of the raw materials are presented in Table 1. VTS primarily consists of SiO_2, CaO, Al_2O_3, TiO_2, and MgO, among which the contents of CaO and SiO_2 are 33.7% and 25.3%, respectively. In addition, the activity coefficient of VTS, $K = W(CaO + MgO + Al_2O_3)/W(SiO_2 + MnO + TiO_2) = 1.299 > 1.2$, indicates that it possesses a certain degree of cementitious activity. Furthermore, the TiO_2 content of VTS is 15.8%, indicating that, compared with other titanium slags, it is a medium-titanium-content waste slag. Table 1 shows that the mass fractions of CaO, SiO_2, and Al_2O_3 in BFS are 41.6%, 30.1%, and 11.5%, respectively, providing reactive Si and Al species. In addition, both VTS and BFS contain SiO_2, CaO, and Al_2O_3, indicating that VTS has a similar pozzolanic (cementitious) activity to BFS. However, the lower mass ratios of SiO_2 and CaO in VTS may lead to lower cementitious activity compared with BFS. The main oxides in SS are CaO, Fe_2O_3, SiO_2, and MgO. In addition, the main oxides in DG are CaO and SO_3. The phase composition of the above raw materials is analyzed in our previous study [20].

Table 1. Chemical composition of raw materials/(wt.%). Adapted from Ref. [20].

Sample	SiO_2	CaO	Al_2O_3	Fe_2O_3	SO_3	MgO	TiO_2	MnO	K_2O	V_2O_5	P_2O_5
VTS	25.3	33.7	11.4	1.6	0.9	9.2	15.8	0.7	0.3	ND	0.1
BFS	30.1	41.6	11.5	2.6	1.3	8.6	1.7	0.3	0.6	ND	0.2
SS	14.0	42.1	3.4	19.4	0.5	9.7	2.2	3.9	0.2	0.9	ND
DG	1.6	49.4	0.3	0.4	46.2	1.1	0.1	ND	ND	ND	ND

The SEM images of VTS are shown in Figure 1. Figure 1a,b present SEM images of unground VTS (particle size 2.36–1.18 mm). It can be observed that the surface of VTS particles contains a small number of pores. Figure 1c shows the surface of unground VTS at higher magnification, where a dense and textured surface is observed. After drying, VTS is ground for 70 min using an SM500 × 500 5 kg laboratory ball mill, achieving a specific surface area of 461.38 m^2/kg. Figure 1d shows its SEM image, which reveals that VTS appears as a black powder containing a small number of particles.

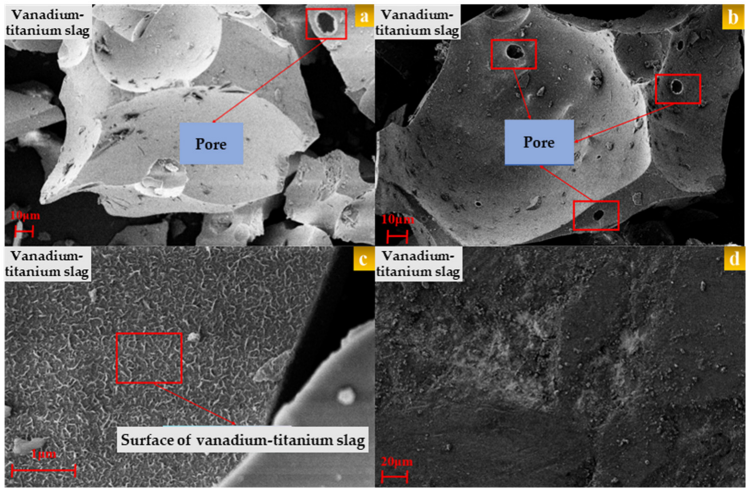


Figure 1. Scanning electron microscope (SEM) image of vanadium–titanium slag; surface close-ups (**a**–**c**); overall morphology (**d**).

2.2. Method

2.2.1. Experimental Ratio Design and Preparation Method

Based on our previous studies [22,23] on the BFS–SS–DG ternary system, the basic mix ratio is first established as BFS:SS:DG = 6:3:1. The effect of VTS content (as a replacement for BFS) on the performance and hydration process of the solid-waste-based cementitious materials is then investigated to determine the optimal replacement level of BFS by VTS. Accordingly, the experimental scheme for the quaternary system is designed as shown in Table 2.

Table 2. Experimental ratio of vanadium–titanium slag content in slurry.

Number	Composition of Cementitious Material (wt. %)				Cementitious Materials Mass (g)	Water-to-Binder Ratio	Water	Total Mass (g)
	VTS	BFS	SS	DG				
A1	0	60	30	10	758	0.32	242	1000
A2	15	45	30	10	758	0.32	242	1000
A3	30	30	30	10	758	0.32	242	1000
A4	45	15	30	10	758	0.32	242	1000
A5	60	0	30	10	758	0.32	242	1000

The specimen preparation method is as follows: the mechanically ground raw materials are weighed according to the designated proportions and placed sequentially into a sample bag, which is shaken for 30 s to achieve preliminary mixing. Then, the cementitious materials and water are added to a cement paste mixer for mechanical stirring. After mixing, the slurry is poured into molds measuring 30 mm × 30 mm × 50 mm. The surface of each specimen is leveled with a steel ruler to ensure smoothness and remove any overflowing slurry. The cast molds are then covered with plastic wrap and allowed to cure at room temperature (20 °C) for 24 h before demolding. After demolding, the prepared cement paste specimens are placed in a standard curing chamber with regular water addition. The compressive strength of the specimens is measured at 3, 7, 28, 90, and 180 days of curing.

2.2.2. Performance and Characterization Methods

The 3, 7, 28, 90, and 180-day compressive strengths of the cement paste specimens are measured following GB/T 17671-2021 [22] "Methods for Strength Testing of Cement Mortar [24]." Toxicity leaching tests are conducted on the 180-day specimens according to the national environmental standard HJ 557-2009 [15] "Leaching Test for Solid Waste—Horizontal Shaking Method [25]."

The hydration heat of the specimens over 7 days is measured using the SHR-8 cement hydration calorimeter (New Castle, DE, USA, TAM Air model) following the national standard GB/T 12959-2008 [15] "Test Methods for Cement Hydration Heat (Direct Method) [26]." X-ray diffraction (XRD) analysis is performed using an Ultima IV diffractometer (Tokyo, Japan, Ultima IV type). XRD is used to identify the mineral phases of hydration products, thereby revealing the types of minerals formed during the hydration process. The chemical bond vibrations of the hydration products are analyzed using a Nicolet iS 10 Fourier transform infrared (FT-IR) spectrometer (Waltham, MA, USA, Nicolet iS 10 model), providing a basis for identifying the chemical structure of the hydration products. Simultaneous thermal analysis (TG–DSC) is performed using a Netzsch STA449C differential thermal analyzer (Selb, Germany, Netzer). The temperature range is 20–1000 °C with a heating rate of 10 °C/min, and nitrogen is used as the carrier gas. X-ray photoelectron spectroscopy (XPS) using a Thermo Scientific ESCALAB 250Xi (East Grinstead, UK, Thermo Kalpha model) is employed to analyze the binding energy spectra of Al 2p, Ca 2p, O 1s, and Ti 2p orbitals. Scanning electron microscopy (SEM) with a Hitachi Regulus8100

(Oberkochen, Germany, Zeiss Supra 55 model) is used to directly observe the microstructure and morphology of the hydration products.

3. Results

3.1. Compressive Strength

Figure 2 shows the uniaxial compressive strength of cement paste specimens with different mix proportions cured for 3, 7, 28, 90, and 180 days. It can be seen that both the VTS content and the curing age have significant effects on the compressive strength of the cement paste specimens. As the proportion of VTS replacing BFS gradually increases, the overall strength of the specimens shows a decreasing trend. With the curing age extended from 3 to 28 days, the compressive strength of specimens with different VTS contents steadily increases, indicating that the hydration reaction continues throughout this period. Among them, the early 3-day compressive strengths of paste specimens A1, A2, and A3 reach 18.39 MPa, 19.29 MPa, and 14.02 MPa, respectively. The 28-day compressive strengths of the specimens are 38.55 MPa, 33.91 MPa, and 31.33 MPa, respectively, all exceeding 30 MPa and meeting the uniaxial compressive strength requirements (>30 MPa) for engineering applications of cementitious materials. Moreover, the strength reduction of A1, A2, and A3 with increasing VTS content is relatively small, generally within the range of 2–4 MPa.

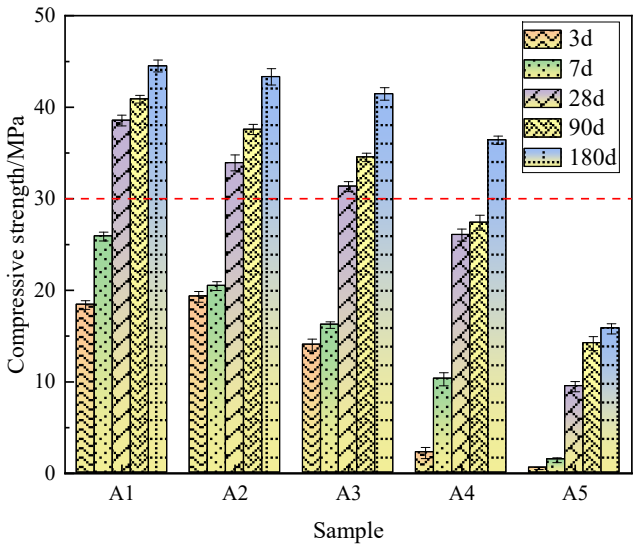


Figure 2. Compressive strength of vanadium–titanium slag-slurry samples at different ages.

With a further increase in VTS content (45–60%), the strength of the specimens deteriorates sharply. For example, the 3-day strength of specimen A4 is only 2.23 MPa, a decrease of 11.79 MPa compared with A3, and its 28-day strength is only 26.03 MPa, failing to meet the 30 MPa target requirement. The performance of A5, which completely replaces BFS, is even worse. Considering the 3-day and 28-day performance of the experimental specimens and aiming to maximize the utilization of VTS, A3 (VTS:BFS:SS:DG = 3:3:3:1) is determined as the optimal mix proportion.

3.2. Toxicity Leaching Safety

Table 3 shows that the specimens exhibit low detectable concentrations of Zn ions, while the leaching concentrations of Pb, As, Ni, Cr, Cd, Hg, Sb, and Cu are very low, even below the detection limits. Therefore, the heavy metal concentrations in the leachate of A1–A5 specimens are all significantly lower than the limits specified in the "Standards for

Drinking Water Quality" (GB 5749-2022) [27]. This indicates that VTS-based cementitious materials have high leaching safety and do not pose a toxic risk to the environment.

Table 3. Heavy metal concentrations in leachate from 28-day hydrated test specimens.

Sample	Zn	Pb	As	Ni	Cr	Cd	Hg	Sb	Cu
	Concentration (μg/L)								
A1	10.54	0.03	0.04	ND	ND	ND	ND	ND	ND
A2	8.12	ND	0.01	ND	0.16	ND	ND	ND	ND
A3	5.61	ND	ND	ND	ND	ND	ND	ND	1.19
A4	9.32	0.06	0.02	ND	0.53	ND	ND	ND	ND
A5	7.87	0.01	ND	ND	ND	ND	0.01	ND	2.65
GB 5749-2022	1000	10	10	20	50	5	1	5	1000

ND stands for "not detected", meaning the result is below the detection limit.

3.3. Hydration Heat Analysis over 168 h

When solid-waste-based cementitious materials are mixed with water, an exothermic reaction occurs, so the hydration heat can be used to study the hydration rate. Based on the trends of the hydration heat curves over different time intervals, the effect of VTS content on the hydration heat of the system under different mix proportions is investigated. Figure 3a shows the hydration heat curves of solid-waste-based cementitious materials A1, A3, and A5. According to the characteristics of the hydration reaction, the heat evolution curve of all-solid-waste cementitious materials can generally be divided into five stages: (1) initial period; (2) induction period; (3) acceleration period; (4) deceleration period; and (5) steady period. Comparing A1, A3, and A5, it is observed that the hydration characteristics of the quaternary system have changed significantly. First, the induction period (second stage) of the quaternary system is shortened, causing the acceleration period (third stage) to arrive earlier. This indicates that the hydration rate is accelerated due to the synergistic effects in the quaternary system. At this stage, under the synergistic action of VTS with BFS, SS, and DG, the curve of the hydration heat release rate for A3 in the quaternary system during the acceleration and deceleration periods is noticeably broader than that of A5 in the ternary system. Long-term observation of the hydration heat curves shows that, upon completion of the hydration reaction, the cumulative hydration heat released by A3 in the quaternary system is much higher than that of A5 in the ternary system. This confirms that VTS undergoes a synergistic reaction with BFS, SS, and DG in the multi-solid-waste system. By fitting the Knudsen equation (Equation (1)) [15], the theoretical ultimate heat release (P_m) and the half-life (t_∂) of the hydration reaction can be calculated. Figure 3b reveals a linear relationship between $1/(t - t_0)$ and $1/P$, indicating that this linear relationship exists during the stable hydration stage. Figure 3c presents the linear fitting results of $1/(t - t_0)$ versus $1/P$, showing that the P_m values of A1, A3, and A5 are 213.68 J/g, 215.52 J/g, and 217.39 J/g, respectively. This indicates that increasing the mass fraction of VTS enhances the theoretical ultimate heat release of the cementitious material, which may be attributed to the "slow hydration" characteristic of VTS. Meanwhile, A5 exhibits the longest half-life (t_∂), reaching 175.29 h, further confirming that V5 has a longer hydration duration. Using Equation (2), the degree of hydration (a) can be calculated. Figure 3d shows that the hydration degrees of A1, A3, and A5 at 168 h are 59.79%, 57.09%, and 46.42%, respectively. This further indicates that A1 exhibits a faster hydration rate in the early stage, whereas A5 shows a slower hydration rate, demonstrating its slow hydration characteristics. Notably, A3 maintains a relatively high hydration heat and heat release rate in the middle and later stages of hydration, demonstrating that VTS gradually and continuously participates in

the hydration reaction under the synergistic activation of BFS, SS, and DG, releasing heat slowly over time.

$$\frac{1}{P} = \frac{1}{P_m} - \frac{t_\partial}{P_m(t - t_0)} \quad (1)$$

$$a = \frac{P}{P_m} \times 100\% \quad (2)$$

In the equation: t_0—time at which the induction period begins (h); P—cumulative heat release of the material at $(t - t_0)$ (J/g); P_m—theoretically calculated ultimate heat release (J/g); t_∂—half-life (h); a—degree of hydration reaction (%).

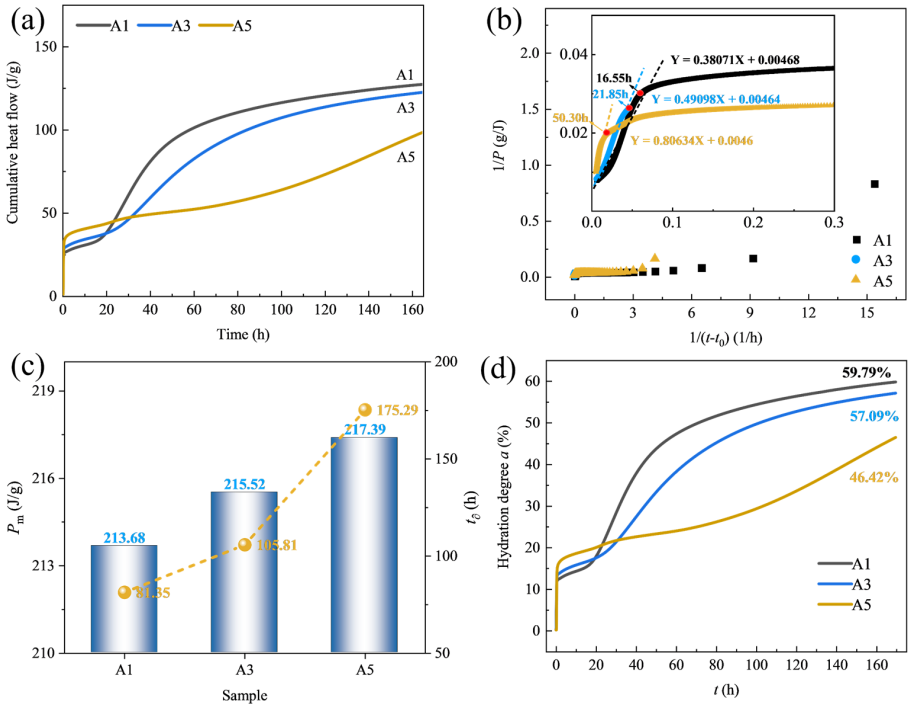


Figure 3. Total amount of heat release from hydration of solid waste based cementitious materials: cumulative hydration exothermic heat released within 168 h (**a**); the relationship between 1/P and 1/(t – t0) (**b**); the theoretical maximum exothermic heat (Pm) and half-life of A1, A3 and A5 (**c**); the degree of hydration of A1, A3 and A5 (**d**).

3.4. Analysis of Hydration Crystalline Phases and Chemical Bond Evolution

3.4.1. Crystalline Phases Analysis

Figure 4 shows the XRD patterns of the hydration products of sample A3 at different curing ages. It can be seen that the main mineral phases of the hydration products in A3 are ettringite (AFt), dicalcium silicate (C_2S), dihydrate gypsum ($CaSO_4 \cdot 2H_2O$), and the RO phase. From the hydration process perspective, diffraction peaks of AFt can already be detected in A3 at 3 days, indicating that the hydration reaction has begun in the early stage. As an important product in cement hydration, the formation of AFt is closely related to the early strength development and stability of cement-based materials. With the extension of the curing period, the intensity of the AFt diffraction peaks gradually increases by day 7, reflecting the ongoing hydration reaction and the increasing content of ettringite. The detection of AFt peaks in A3 at three days indicates that hydration has already started at an early stage. As a hydration product, AFt formation is closely related to the early strength and stability of the specimens. By day seven, the peak intensity slightly increases, suggesting that the AFt crystals are more complete than at three days and likely to continue to grow. By day 28, the diffraction peak intensity further increases, indicating that with

longer curing, the AFt crystals in A3 become more complete, and the formation of AFt increases, predominantly occurring in the middle to later stages of hydration. The "bulging" observed between 25° and 35° in the figure indicates the presence of amorphous C–S–H and C–A–S–H in the A3 cement paste. Since these are amorphous phases, the bulge between 25° and 35° is not very pronounced.

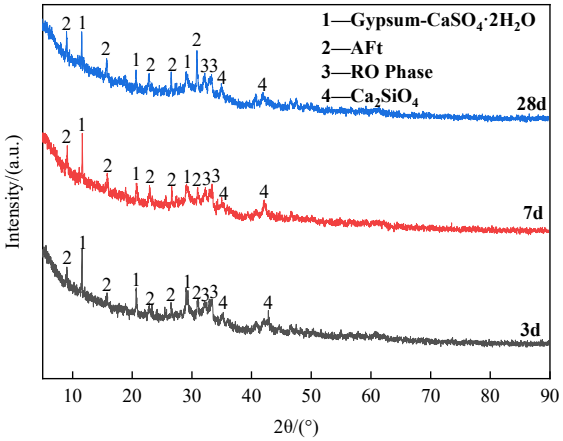


Figure 4. XRD patterns of sample A3 at different curing ages.

No diffraction peaks of tricalcium silicate (C_3S) are observed in the hydration products of A3, indicating that C_3S has fully hydrated to form C–S–H and $Ca(OH)_2$. At three days, diffraction peaks of dicalcium silicate (C_2S) are observed, and their intensity gradually decreases by day seven. By day 28, the peak intensity further decreases, indicating a reduction in C_2S content due to its hydration, producing additional C–S–H and $Ca(OH)_2$. However, no diffraction peaks of $Ca(OH)_2$ are observed in the spectra because it is continuously consumed by the glassy phases in VTS and slag with latent hydraulic activity, providing an alkaline environment and forming C–S–H, C–A–S–H, and AFt. $CaSO_4{\cdot}2H_2O$ is the main component of desulfurization gypsum. In A3 at three days, distinct diffraction peaks of $CaSO_4{\cdot}2H_2O$ can be observed. As the curing age increases, the intensity of these peaks gradually decreases, especially from 7 to 28 days, showing significant changes. This indicates that under alkaline activation, desulfurization gypsum continuously participates in the hydration reaction to form AFt, and the middle to late-stage hydration is vigorous, thereby ensuring the continuous increase in the compressive strength of A3. This is consistent with the reactivity test results of VTS. The RO phase is an inert mineral in SS and therefore does not participate in the hydration reaction.

3.4.2. Chemical Bond Analysis

Figure 5 shows the FT-IR spectra of A3 cement paste at 3, 7, and 28 days of hydration. The peaks at 3404.38 cm^{-1} and 1620.65 cm^{-1} correspond to the O–H stretching and bending vibrations of crystallized water in C–S–H and AFt, respectively. Their transmittance decreases at 7 and 28 days. As hydration progresses, the increase in the number of O–H bonds in the crystallized water of A3 leads to greater absorption at the corresponding infrared wavelengths. This indicates that the middle to late-stage hydration of A3 is vigorous, with a continuous increase in hydration products, which is consistent with the XRD analysis results. The absorption peak at 1427.25 cm^{-1} corresponds to the vibration of [CO_3^{2-}] [28], and its intensity decreases by 28 days, indicating that it is largely consumed during the middle to late stages of hydration. The absorption peak at 1116.17 cm^{-1} corresponds to the vibration of [SO_4^{2-}] [29], and its intensity continuously decreases at 7 and 28 days, showing that [SO_4^{2-}] is extensively consumed during the middle to late hydration stages, meaning that DG continuously participates in the hydration reaction

during this period. The absorption peak at 974.93 cm^{-1} corresponds to the vibration of the Si–O bond in the silicate tetrahedron [19]. In the raw materials, Si–O bonds are mainly present in the glassy phases of VTS and slag as well as in C_2S and C_3S in steel slag. Additionally, the Si–O bond in silicate tetrahedra is a characteristic peak of the hydration product C–S–H, indicating the formation of C–S–H in the system. As the curing age increases, the transmittance of this characteristic peak decreases, indicating that C–S–H is extensively formed during the middle to late stages of hydration and its degree of polymerization continuously increases, gradually forming a network structure. The absorption peaks at 606.08 cm^{-1} and 463.16 cm^{-1} correspond to the symmetric stretching vibrations of Si–O–Al bonds. The transmittance at these peaks remains nearly unchanged at 7 days but disappears after 28 days, indicating the breakage of Si–O–Al bonds.

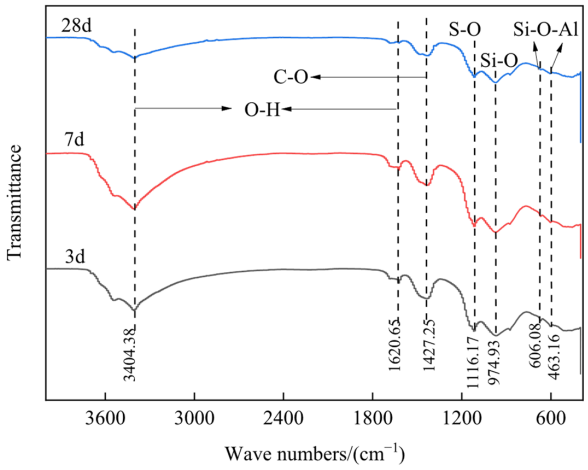


Figure 5. FT-IR spectra of sample A3 at different curing ages.

3.4.3. Analysis of Weight Loss of Hydration Products

Figure 6 shows the TG–DTG curves of A3. The DTG curve indicates that at 3 days, A3 exhibits weight loss peaks at 98 °C, 125 °C, 772 °C, and 860 °C. At 28 days, the A3 cement paste shows weight loss peaks at 106 °C, 125 °C, 770 °C, and 872 °C. At 3 days, the weight loss peak at 98 °C corresponds to the dehydration of C–S–H, C–A–S–H, and AFt in A3, with a weight loss of 2.73%. The peak at 125 °C is due to the dehydration of dihydrate gypsum ($CaSO_4 \cdot 2H_2O$) transforming into hemihydrate gypsum, with a weight loss of 1.34%. At 28 days, the weight loss peak at 106 °C is due to the dehydration of C–S–H, C–A–S–H, and AFt in A3 [30], with a weight loss of 4.85%, which is higher than the total dehydration of C–S–H, C–A–S–H, and AFt at 3 days (4.07%). This indicates that the total amount of hydration products formed at 28 days is greater than that at 3 days. The DTG curve of A3 shows a weak weight loss peak near 554 °C corresponding to $Ca(OH)_2$, indicating that only a small amount of $Ca(OH)_2$ is present in the system, which is consistent with the previous analysis. Both the 3-day and 28-day samples show significant weight loss around 770 °C, which is attributed to the dehydroxylation of hydrated calcium silicate minerals during heating, combined with CO_2 release from carbonate minerals. A heat release peak is observed near 820 °C without significant weight loss, indicating that C–S–H undergoes a phase transformation at this temperature, forming β-wollastonite [31].

The TG curve shows that the weight loss below 200 °C is due to the dehydration of hydration products, indicating the formation of C–S–H, C–A–S–H, and AFt. The weight loss of A3 at 3 days is 14.84%, while at 28 days it is 16.56%. The higher weight loss at 28 days compared to 3 days indicates that hydration products continue to form as the hydration reaction progresses, contributing to the continuous strength increase in the VTS-based cementitious system.

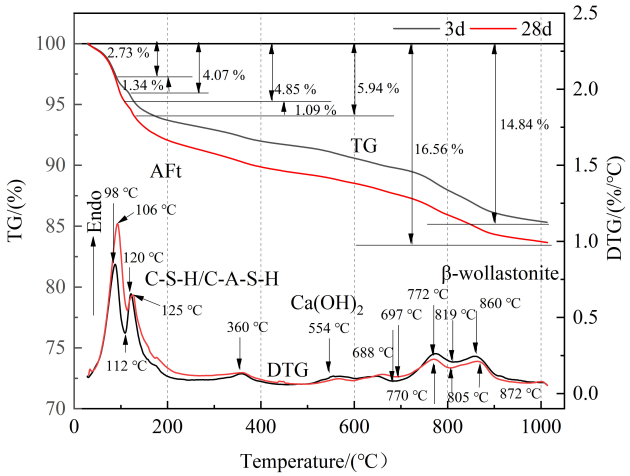


Figure 6. Comparison of TG-DTG spectra of sample A3 hydration at 3 d and 28 d ages.

3.4.4. Chemical Element Orbitals Analysis

Changes in binding energy reflect the chemical environment and bonding state of elements in their hydration products. Figure 7 shows the binding energy spectra of the Al 2p, Ca 2p, O 1s and Ti 2p orbitals for sample A3 after 3 and 28 days of hydration. With the extension of the curing age, the binding energies of Al, Ca, O, and Ti in sample A3 all show an increasing trend. The Al 2p binding energy increases from 75.51 eV to 75.72 eV, Ca 2p from 348.62 eV to 349.46 eV, O 1s from 532.55 eV to 533.27 eV, and Ti 2p from 459.58 eV to 460.19 eV. In summary, the increase in binding energy is attributed to the ongoing hydration reaction, during which VTS and BFS release free [SiO_4] and [AlO_4] units. These units react with Ca^{2+} and SO_4^{2-} ions in the system to form AFt, C–S–H, and C–A–S–H. The dissociation and re-polymerization of [SiO_4] and [AlO_4] units are the main reasons for the increase in the Al 2p binding energy [30]. The formation of AFt is the reason for the increase in the Ca 2p and O 1s binding energies. As a typical complex salt hydration product, the oxygen atoms in the AFt structure mainly exist in the form of oxides and have high electron affinity. This is due to the covalent or ionic bonds formed between oxygen atoms and metal ions such as calcium and aluminum. This bonding state enhances the electron-attracting ability of the oxygen atoms, leading to an increase in the O 1s binding energy.

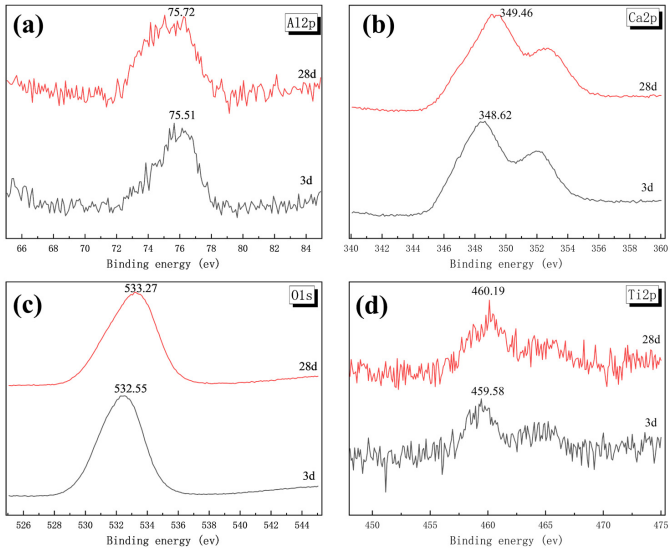


Figure 7. XPS spectra of sample A3 hydration at 3 d and 28 d: Al 2p orbital (**a**); Ca 2p orbital (**b**); O 1s orbital (**c**); Ti 2p orbital (**d**).

3.4.5. Microstructural Analysis

Figure 8 shows the SEM images of A3 cement paste at 3, 7, and 28 days of curing. From Figure 8a,b, it can be observed that hydration has already occurred at 3 days, with needle-like AFt and flocculent C–S–H products beginning to interweave and encapsulate each other, providing early compressive strength for A3. From Figure 8c,d, it can be seen that at 7 days of hydration, the amounts of ettringite (AFt), C–S–H, and C–A–S–H in A3 increase significantly. AFt interweaves between C–S–H and C–A–S–H gels, while unreacted VTS particles adhere to their surfaces. The interlacing of these phases creates a denser structure, contributing to the increase in the compressive strength of A3. From Figure 8e,f, it can be observed that at 28 days of hydration, the structure of A3 becomes even denser, and the amount of hydration products further increases. C–S–H and C–A–S–H form a network structure interwoven with root-like AFt, with multiple layers encapsulating each other. Short-column AFt intersperses within this matrix, further filling the pores of the cementitious system, making the structure more stable and contributing to the continued increase in the compressive strength of A3. This confirms that the quaternary system of VTS, BFS, SS, and DG undergo a synergistic multi-solid-waste reaction, promoting the formation and growth of hydration products, and further demonstrates that the VTS-based cementitious material exhibits vigorous hydration in the middle to late stages.

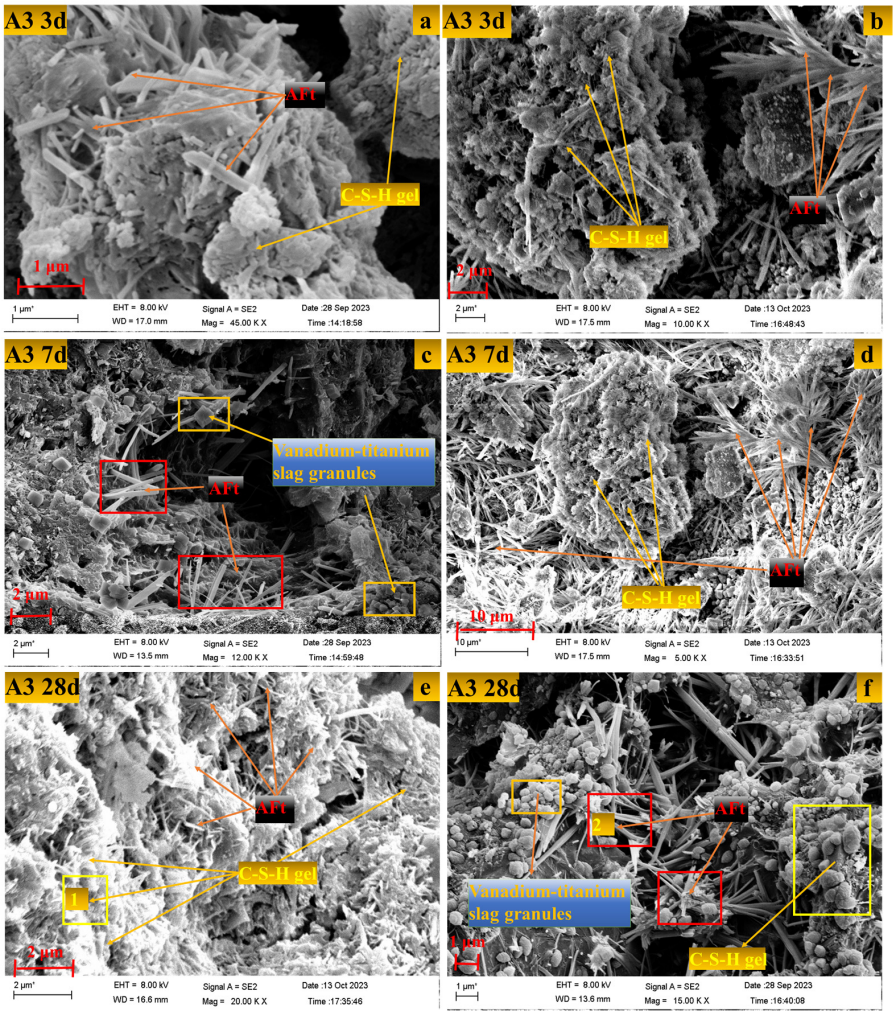


Figure 8. Morphology of hydration products at different ages of A3 slurry test blocks: 3 days after hydration (**a**,**b**); 7 days after hydration (**c**,**d**); 28 days after hydration (**e**,**f**).

Figure 9 shows the EDS spectra of A3 cement paste at 28 days of curing. Table 4 presents the elemental analysis of points 1 (Figure 8e) and 2 (Figure 8f). As observed in Figure 8, the microstructure of the hydration products in A3 consists of short-column hydration products interwoven and encapsulated with flocculent hydration products layer by layer. Based on the EDS analysis of points 1 and 2, combined with the previous XRD and FT-IR results, it can be concluded that the needle-like products are AFt, the flocculent products are C–S–H and C–A–S–H, and the granular products are unreacted VTS particles.

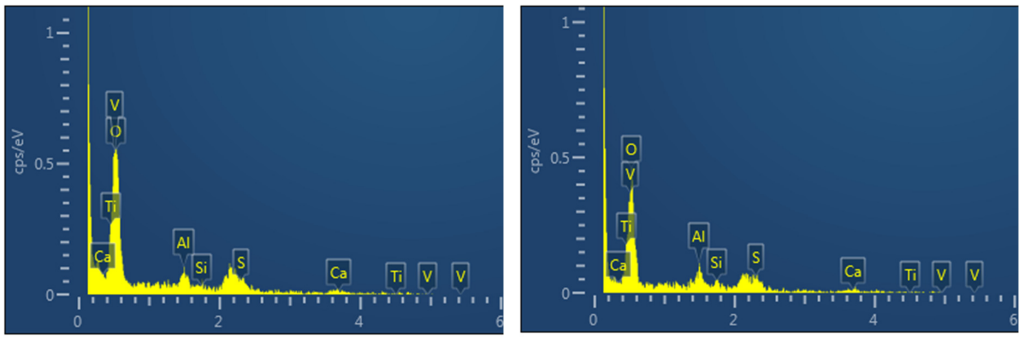


Figure 9. EDS spectra at points 1 and 2 in A3-28d.

Table 4. Mass ratio of each component/wt.%.

Position	Mass Fraction of Each Component						
	O	Mg	Al	Si	S	Ca	Ti
1	53.15	0.00	11.06	7.15	8.56	23.53	0.00
2	65.37	0.00	7.49	4.34	3.91	18.89	0.00

4. Discussion

The incorporation of VTS significantly alters the hydration kinetics and product evolution pathways of the BFS–SS–DG ternary system. Hydration heat analysis shows that the A3 specimen with 30% VTS maintains a relatively high heat release rate in the middle to late stages of hydration (after 72 h), and its cumulative heat release is significantly higher than that of the A5 specimen without VTS. In addition, XPS analysis shows that with increasing curing age, the binding energies of Al 2p, Ca 2p, and O 1s all exhibit an upward trend, with the Al 2p binding energy increasing from 75.51 eV to 75.72 eV. This phenomenon reveals the unique "slow-release" effect of VTS: its stable glassy structure undergoes only surface depolymerization in the early stage. However, as hydration progresses, the alkalinity of the system continuously increases and Ca^{2+} keeps entering the solution, promoting the gradual dissociation of the $[SiO_4]$–$[AlO_4]$ network within VTS. This releases more reactive silicate and aluminate units to participate in subsequent hydration reactions, and the depolymerization–repolymerization process facilitates the restructuring of Al–O and Si–O bonds. XRD analysis confirms that the intensity of AFt diffraction peaks in the A3 specimen which continuously increases from 7 to 28 days. TG–DTG results show that the weight loss of C–S–H/AFt at 28 days (4.85%) is significantly higher than that at 3 days (2.73%), further verifying the continuous formation of hydration products in the middle to late stages. The hydration degree analysis shows that the hydration degrees of A1, A3, and A5 at 168 h are 59.79%, 57.09%, and 46.42%, respectively (Figure 3d), demonstrating that VTS-based cementitious systems with higher mass fractions exhibit slower hydration rates and pronounced slow hydration characteristics. This "slow-release" mechanism enables a time-dependent synergy between VTS and BFS, in which VTS ensures the continuous progression of the hydration reaction during the middle and later stages,

thereby promoting the formation and growth of C–(A)–S–H gel and AFt crystals. AFt acts as a structural framework, while the C–(A)–S–H gel binds AFt, VTS, and matrix particles together. This densified microstructure optimizes the strength development pattern of the system. The chemical reaction equations of C–S–H, C–A–S–H, and AFt are shown in Equations (3)–(5).

$$Ca(OH)_2 + SiO_2 + H_2O \rightarrow C\text{-}S\text{-}H \quad (3)$$

$$Ca(OH)_2 + Al_2O_3 + SiO_2 + (n-1)H_2O \rightarrow CaO{\bullet}SiO_2{\bullet}Al_2O_3{\bullet}nH_2O\ (C\text{-}A\text{-}S\text{-}H) \quad (4)$$

$$3Ca(OH)_2 + Al_2O_3 + 3(CaSO_4{\bullet}2H_2O) + 23H_2O \rightarrow 3CaO{\bullet}Al_2O_3{\bullet}3CaSO_4{\bullet}32H_2O\ (AFt) \quad (5)$$

It is worth noting that the Ti 2p binding energy also increases from 459.58 eV to 460.19 eV, suggesting that the TiO_2 component may participate in the formation of hydration products or alter the surface chemical environment. Combined with SEM–EDS observations, in the A3-28d sample, short-column AFt crystals and flocculent C–S–H gels form a dense interwoven network structure, while unreacted VTS particles are covered with a large amount of hydration products. This indicates that, under appropriate addition levels, fine VTS particles can exert both micro-filling and heterogeneous nucleation effects within the system. Fine VTS particles can fill the pores in the cementitious system, enhancing particle packing density and providing more nucleation sites for the deposition of hydration products. This promotes the formation and growth of C–(A)–S–H gels and AFt crystals, leading to a more uniform distribution of hydration products within the matrix. The crystal nucleation interface effect provided by VTS particles is consistent with the crystal growth surface area and interfacial phenomena reported by Khormali [32]. This microstructural densification effect improves the structural stability of the system and, to some extent, enhances its mechanical properties (with a compressive strength of 31.33 MPa for A3 at 28 days). However, when the VTS content exceeds 45%, the strength of the system deteriorates sharply. The XRD results show a significant decrease in the intensity of AFt diffraction peaks, and the microstructure becomes loose and porous. This indicates that the "slow-release" effect of VTS requires an appropriate alkaline environment and sufficient active silicon and aluminum sources as support. Excessive replacement of BFS reduces the amount of highly reactive silico-aluminate components in the system, thereby weakening the formation basis of AFt and C–S–H.

In summary, compared with other supplementary cementitious materials, the presence of TiO_2 in VTS enhances the stability of its glassy structure, resulting in relatively low early-stage reactivity. However, this structural characteristic provides a unique advantage for sustained middle- to late-stage hydration, as the gradual release of VTS activity is closely related to the depolymerization kinetics of its internal $[SiO_4]$–$[AlO_4]$ network. When the VTS content is controlled within 30%, it forms a good synergistic activation effect with BFS and SS, resulting in abundant hydration products with a high degree of crystallinity. Figure 10 illustrates the schematic of the hydration reaction of VTS. However, this work still has several limitations. First, the long-term durability of the material under practical engineering conditions should be evaluated, for example, its resistance to sulfate attack or carbonation over 360 days when applied in actual underground goaf backfilling and curing scenarios. Second, due to the high TiO_2 content, which inhibits the hydration reaction in the early stage (within 3 days), it is necessary to explore new green approaches, such as chemical activation or thermal treatment, to enhance the initial reactivity of VTS.

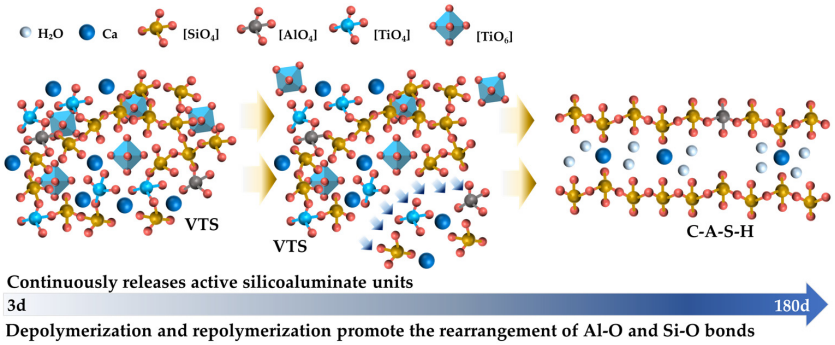


Figure 10. Schematic representation of the hydration reaction of VTS.

5. Conclusions

In this study, VTS was used to partially replace BFS to construct a VTS–BFS–SS–DG quaternary all-solid-waste cementitious system. The effects of VTS content on the system's performance, hydration behavior, product evolution, and microstructure were systematically investigated, leading to the following main conclusions:

(1) The VTS content has a significant regulatory effect on the mechanical performance of the system. When VTS replaces 30% of BFS (A3, VTS:BFS:SS:DG = 3:3:3:1), the system exhibits the optimal overall performance, with a 28-day compressive strength of 31.33 MPa, meeting the engineering requirement (>30 MPa). Excessive addition (≥45%) leads to a sharp decrease in strength, attributed to the reduced content of highly reactive BFS, which weakens the foundation for hydration product formation.

(2) The leaching concentrations of heavy metals in all specimens are far below the limits specified in the "Standards for Drinking Water Quality" (GB 5749-2022), indicating good environmental safety.

(3) VTS exhibits a relatively slow hydration rate in the early stage, showing a unique "gradual release" hydration mechanism within the system. Hydration heat analysis indicates that the A3 specimen maintains a relatively high heat release rate in the middle to late stages of hydration (after 72 h), and the cumulative hydration heat is significantly higher than that of the control system without VTS. Furthermore, the intensity of AFt diffraction peaks and the weight loss of C–S–H/AFt continue to increase from 7 to 28 days, indicating that the middle-to-late-stage activity of VTS effectively sustains the hydration reaction. The dissociation and re-polymerization of $[SiO_4]$ and $[AlO_4]$ units promote the reorganization of Al–O and Si–O bonds.

(4) Under appropriate addition levels, fine VTS particles can not only optimize particle gradation through micro-filling effects but also act as heterogeneous nucleation sites to promote the deposition of hydration products, thereby improving the uniformity and density of the microstructure to some extent. The TiO_2 component may participate in the chemical environment evolution of the hydration products. However, excessive VTS content significantly increases the TiO_2 proportion, causing some particles to remain inert during hydration, which markedly inhibits the overall hydration reaction rate.

(5) Future studies can further explore the regulatory mechanism of TiO_2 on the chemical composition of C–S–H and systematically evaluate the engineering applicability of this system through long-term durability tests.

Author Contributions: Conceptualization, B.S. and X.X.; methodology, T.Z.; software, J.L.; validation, B.S., X.X. and T.Z.; formal analysis, S.Z.; investigation, X.X.; resources, B.S.; data curation, X.X.; writing—original draft preparation, B.S.; writing—review and editing, S.Z.; visualization, X.X.; supervision, B.S.; project administration, S.Z. and H.Y.; funding acquisition, S.Z. All authors have read and agreed to the published version of the manuscript.

Funding: This research was funded by the Guizhou Provincial Science and Technology Program Project, grant number Qian Ke He Zhong Yin Di (2025) 011.

Data Availability Statement: The data presented in this study are available on request from the corresponding author. The data are not publicly available due to privacy restrictions.

Conflicts of Interest: The authors declare no conflicts of interest.

Abbreviations

VTS	Vanadium–titanium slag
BFS	blast furnace slag
SS	Steel slag
DG	Desulfurization gypsum
XRD	X-ray diffraction
FT-IR	Fourier-transform infrared spectroscopy
TG–DSC	Thermogravimetric analysis
XPS	X-ray photoelectron spectroscopy
SEM	Scanning electron microscopy

References

1. Zhang, S.S.; Wang, Z.Y.; Peng, H.; Hu, P.; Rao, J.T.; Zhang, J.L.; Pang, J. Distribution behavior of vanadium and titanium between hot metal and high titanium slag relevant to HIsmelt smelting condition. *J. Mater. Res. Technol.* **2022**, *19*, 4517–4524. [CrossRef]
2. Ma, X.M.; Xu, L.; Cai, J.M.; Zhang, Z.Y.; Sun, Y.Q.; Zhu, W.W.; Pan, J.L. Feasible use of titanium slag in improving properties of low carbon fire-resistive cementitious composites at elevated temperatures. *Constr. Build. Mater.* **2024**, *416*, 135272. [CrossRef]
3. Li, C.H.; Du, P.P.; Zhang, J.S.; Zhao, S.X.; Gao, M.L.; Wang, Q.H.; Tian, T.L.; Li, L.J.; Long, Y. Advances in Integrated Extraction of Valuable Components from Ti-Bearing Slag. *Metals* **2025**, *15*, 1080. [CrossRef]
4. Rui, Y.F.; Li, N.; Tang, R.F.; Zhao, S.X.; Zhang, X.; Zhao, S.W.; Zheng, Y.C.; Huang, T.Y. The influence of vanadium titanium slag and blast furnace slag on the properties of cement-based materials: Fluidity, mechanical properties, and hydration. *Constr. Build. Mater.* **2025**, *504*, 144679. [CrossRef]
5. Hou, X.K.; Wang, D.; Shi, Y.M.; Guo, H.T.; He, Y.Y. Hydraulic Activity and Microstructure Analysis of High-Titanium Slag. *Materials* **2020**, *13*, 1239. [CrossRef] [PubMed]
6. Liu, Z.; Lai, Z.Y.; Luo, X.Z.; Xiao, R.; Liu, M.L.; Deng, Q.B.; Chen, J.W.; Lu, Z.Y.; Lv, S.Z. Effect of titanium slag on the properties of magnesium phosphate cement. *Constr. Build. Mater.* **2022**, *343*, 128132. [CrossRef]
7. Liu, G.; Li, M.; Zhang, S.P.; Zhang, Z.H.; Wu, Y.P. Strengthening effect and mechanism of titanium extraction slag on the mechanical property of calcium aluminate cement. *Ceram. Int.* **2023**, *49*, 30326–30334. [CrossRef]
8. Wang, W.; Li, X.S.; Shen, J.A.; Zhu, H.Z.; Wang, J. Feasibility of high titanium heavy slag used as aggregates for asphalt mixtures. *J. Clean. Prod.* **2023**, *411*, 137332. [CrossRef]
9. Bai, C.Y.; Deng, Y.; Zhou, Q.; Deng, G.; Yang, T.T.; Yang, Y.Y. Effect of different curing methods on the preparation of carbonized high-titanium slag based geopolymers. *Constr. Build. Mater.* **2022**, *342*, 128023. [CrossRef]
10. Li, X.; Jun, L.; Lu, Z.; Hou, L.; Chen, J. Preparation and properties of reactive powder concrete by using titanium slag aggregates. *Constr. Build. Mater.* **2020**, *234*, 117342. [CrossRef]
11. He, K.; Deng, Y.; Cao, Z.Q.; Zhang, X.F. Engineering performance and microscale structure of activated high titanium slag-soil-cement-bentonite (HTS-SCB) slurry backfill. *Constr. Build. Mater.* **2023**, *373*, 130776. [CrossRef]
12. Wei, H.; Chen, A.Y.; Li, C.H.; Zhang, J.M.; Lu, H. Response Surface Optimization of High-Durability Fly Ash–Slag Blended Concrete as an Eco-Friendly Repair Material. *Materials* **2026**, *19*, 1058. [CrossRef]
13. Fathi, M.E.; El-Zoughiby, M.E.; Mortagi, M.; Youssf, O.; Abdulazeez, M.; Tahwia, A.M. Shear Performance of Sustainable Self-Compacting Geopolymer RC Beams: Experimental and Numerical Study. *Infrastructures* **2026**, *11*, 84. [CrossRef]
14. Ma, Z.; Pu, C.; Zhang, G.H.; Wang, B.; Litifu, W.; Liu, C.M.; Li, S.H.; Yin, P. Study on the Influence of Modified Steel Slag Filler on the Rheological Properties and Moisture Stability of Asphalt Mastic. *Coatings* **2026**, *16*, 340. [CrossRef]
15. Zhang, S.Q.; Zhao, T.; Li, K.Q.; Ni, W.; Yang, H.F.; Wu, Z.P.; Li, J.; Li, Y.; Zhang, B.; Wang, J.J.; et al. Effect of blast furnace slag substitution for cement in carbon-reduced and low-cost solidified/stabilized cementitious materials. *Green Smart Min. Eng.* **2024**, *1*, 104–117. [CrossRef]
16. Zhang, S.Q.; Shi, T.Y.; Ni, W.; Li, K.Q.; Gao, W.; Wang, K.; Zhang, Y.Y. The mechanism of hydrating and solidifying green mine fill materials using circulating fluidized bed fly ash-slag-based agent. *J. Hazard. Mater.* **2021**, *415*, 125625. [CrossRef]

17. Xu, Z.Q.; Hu, X.J. Characteristics of Steel Slag and Properties of High-Temperature Reconstructed Steel Slag. *Metals* **2026**, *16*, 85. [CrossRef]
18. Li, Z.H.; Yao, J.; Hua, S.G.; Li, S.Q.; Li, K.X.; Ma, B. An Innovative High-Content Steel Slag Alkali-Sulfate Composite Activated Binder: Hydration Behavior and Application. *Materials* **2026**, *19*, 936. [CrossRef] [PubMed]
19. Zhao, T.; Zhang, S.Q.; Yang, H.F.; Ni, W.; Li, J.; Zhang, G.; Teng, G.X.; Li, X.; Guo, S.; Zhou, Y.C.; et al. Leaching and hydrating mechanisms, economic benefits of backfill materials by using coal fly ash–slag-based binder for environmentally sustainable production. *Constr. Build. Mater.* **2023**, *397*, 132360. [CrossRef]
20. Liu, J.Y.; Zhang, S.Q.; Yang, H.F.; Ni, W.; Guan, D.S.; Xu, X.Y.; Zhan, Y. Influence of Vanadium-Titanium Slag Substitution on Properties and Microstructure of Blast Furnace Slag-Steel Slag-Desulfurization Gypsum Gel System. *Gels* **2026**, *12*, 3. [CrossRef]
21. *GB/T 208-2014*; Test Method for Density of Cement (Standard). China Standards Press: Beijing, China, 2014.
22. Chen, X.Y.; Zhang, S.Q.; Ni, W.; Zhao, T.; Li, Y.Y. Dual role of FGD ash in GBFS-steel slag-FGD gypsum-FGD ash quaternary system: Hydration acceleration and strength enhancement mechanisms. *Constr. Build. Mater.* **2025**, *497*, 143948. [CrossRef]
23. Zhan, Y.; Zhang, S.Q.; Yang, X.; Li, K.Q.; Zhang, B.; Zhao, T.; Li, G.C.; Ye, L.F.; Wu, S.; Ni, W. Research on the Mechanical Properties, Hydration Mechanism and Engineering Applications of Road Base Materials Prepared from Harmless-Treated Barium Slag and Multiple Industrial Solid Wastes. *Appl. Sci.* **2026**, *16*, 74. [CrossRef]
24. *GB/T 17671-2021*; Test Method of Cement Mortar Strength (ISO Method). China Standard Press: Beijing, China, 2021.
25. *HJ 557-2010*; Solid Waste—Extraction Procedure for Leaching Toxicity—Horizontal Vibration Method. China Environmental Science Press: Beijing, China, 2010.
26. *GB/T 12959-2008*; Test Method for Heat of Hydration of Cement. China Standard Press: Beijing, China, 2008.
27. *GB 5749-2022*; Standards for Drinking Water Quality. Standardization Administration of China: Beijing, China, 2022.
28. Li, N.; Farzadnia, N.; Shi, C.U. Microstructural changes in alkali-activated slag mortars induced by accelerated carbonation. *Cem. Concr. Res.* **2017**, *100*, 214–226. [CrossRef]
29. Kapeluszna, E.; Kotwica, Ł.; Różycka, A.; Gołek, Ł. Incorporation of Al in C-A-S-H gels with various Ca/Si and Al/Si ratio: Microstructural and structural characteristics with DTA/TG, XRD, FTIR and TEM analysis. *Constr. Build. Mater.* **2017**, *155*, 643–653. [CrossRef]
30. Zou, Y.X.; Zuo, X.B.; Yin, G.J.; Zhang, H.L.; Ding, F.B. Utilization of industrial wastes on the durability improvement of cementitious materials: A comparative study between FA and GGBFS. *Constr. Build. Mater.* **2024**, *421*, 135629. [CrossRef]
31. El-Didamony, H.; Amer, A.A.; El-Sokkary, T.M.; Abd-El-Aziz, H. Effect of substitution of granulated slag by air-cooled slag on the properties of alkali activated slag. *Ceram. Int.* **2013**, *39*, 171–181. [CrossRef]
32. Khormali, A. Using a New Mixture of Reagents for Effective Inhibition of Corrosion and Salt Precipitation in the Petroleum Industry. *J. Chem. Pet. Eng.* **2021**, *55*, 257–276.

Disclaimer/Publisher's Note: The statements, opinions and data contained in all publications are solely those of the individual author(s) and contributor(s) and not of MDPI and/or the editor(s). MDPI and/or the editor(s) disclaim responsibility for any injury to people or property resulting from any ideas, methods, instructions or products referred to in the content.